

Numerical approaches for calculating the low-field dc Hall coefficient of the doped Hubbard model

Wen O. Wang,^{1,*} Jixun K. Ding,¹ Brian Moritz,² Yoni Schattner,^{2,3} Edwin W. Huang,⁴ and Thomas P. Devereaux^{2,5,†}

¹*Department of Applied Physics, Stanford University, Stanford, CA 94305, USA*

²*Stanford Institute for Materials and Energy Sciences, SLAC National Accelerator Laboratory, 2575 Sand Hill Road, Menlo Park, CA 94025, USA*

³*Department of Physics, Stanford University, Stanford, CA 94305, USA*

⁴*Department of Physics and Institute of Condensed Matter Theory, University of Illinois at Urbana-Champaign, Urbana, IL 61801, USA*

⁵*Department of Materials Science and Engineering, Stanford University, Stanford, CA 94305, USA*

(Dated: July 13, 2021)

Using determinant Quantum Monte Carlo, we compare three methods of evaluating the dc Hall coefficient R_H of the Hubbard model: the direct measurement of the off-diagonal current-current correlator χ_{xy} in a system coupled to a finite magnetic field (FF), χ_{xy}^{FF} ; the three-current linear response to an infinitesimal field as measured in the zero-field (ZF) Hubbard Hamiltonian, χ_{xy}^{ZF} ; and the leading order of the recurrent expansion $R_H^{(0)}$ in terms of thermodynamic susceptibilities. The two quantities χ_{xy}^{FF} and χ_{xy}^{ZF} can be compared directly in imaginary time. Proxies for R_H constructed from the three-current correlator χ_{xy}^{ZF} can be determined under different simplifying assumptions and compared with $R_H^{(0)}$. We find these different quantities to be consistent with one another, validating previous conclusions about the close correspondence between Fermi surface topology and the sign of R_H , even for strongly correlated systems. These various quantities also provide a useful set of numerical tools for testing theoretical predictions about the full behavior of the Hall conductivity for strong correlations.

I. INTRODUCTION

Transport measurements are among the most common and accessible experimental probes, and are often among the first to be performed following the discovery of new materials. Yet, the theoretical investigation of normal state transport properties of quantum materials presents a number of unique challenges. Fermi liquid theory and the associated Boltzmann transport theory, which provide the theoretical framework for the understanding of ordinary metals, are known to break down in certain regimes. In the case of the high- T_c cuprates, this is evidenced by the linear-in- T longitudinal resistivity, which violates the Mott-Ioffe-Regel (MIR) limit and has been synonymous with what has been called “strange metallicity” [1–7]. In addition, the Hall coefficient R_H for cuprates has a strong temperature dependence [8, 9], in contrast to predictions of Fermi liquid theory.

The Hubbard model, despite its simple form, successfully captures some of the non-Fermi liquid signatures in the normal state of cuprates. Strange metallic resistivity, without a signature of saturation at the MIR limit, has been successfully observed in the Hubbard model, both numerically [10] via determinant quantum Monte Carlo (DQMC) [11, 12] simulations and in cold atoms experiments [13, 14]. R_H investigated in another recent DQMC work [15] also shows strong temperature dependence and

a non-trivial peak at temperature $T \sim t$, the kinetic energy scale, which may be connected to the rise of R_H in cuprates like LSCO as temperature decreases from the ultra high temperature limit [16]. The close relationship between the experimental observations of cuprates and the theoretical results from the Hubbard model motivate us to continue investigating transport properties of the Hubbard model, specifically R_H . We seek to better understand novel transport phenomena in materials without quasiparticles, and the relationship to the evolution of the electronic structure for understanding intertwined phases in the cuprates [17].

A calculation of the Hall coefficient is more complex compared to the longitudinal resistivity. Previous works have investigated R_H in the $t - J$ and Hubbard models for both high frequency and dc limits [18–24]; however, much of the work for strongly correlated models has involved certain simplifying assumptions, approximations, and limiting cases [22, 25]. A faithful comparison of methods that can be used to calculate the dc Hall coefficient in a strongly correlated framework has been lacking.

Measuring R_H in a numerically exact way poses challenges, limited by both the speed and efficiency of numerical techniques. For example, exact diagonalization is restricted to small lattice sizes [26]; density-matrix renormalization group (DMRG) is limited to a small number of excited states and may not be stable for calculating transport properties of 2D systems, especially in the metallic phase [27]. Numerical simulations for larger lattice sizes can be performed using quantum Monte Carlo (QMC)

* wenwang.physics@gmail.com

† tpd@stanford.edu

simulations in imaginary time for temperatures where the fermion sign problem is not too severe [28]. In the work presented here we use DQMC, a particular flavor of QMC.

One approach for obtaining $R_H = -B^{-1}\rho_{xy}$ via QMC simulations is to explicitly couple the Hubbard model to a finite magnetic field. Current-current correlators $\chi_{\alpha\beta}(\tau)$ ($\alpha, \beta = x$ or y direction) measured in imaginary time are then analytically continued to real frequency to obtain all components of the conductivity tensor $\sigma_{\alpha\beta}(\omega)$. In this approach, explicitly adding a magnetic field B raises the computational complexity by requiring complex (as opposed to real) calculations. Apart from the inherent difficulty in properly incorporating the magnetic field B due to considerations of gauge invariance, this procedure also suffers from the need to analytically continue both the diagonal and off-diagonal components of $\sigma_{\alpha\beta}$ concurrently [29, 30].

In an alternative approach, one could consider the zero-field limit by expanding the off-diagonal part of $\chi_{\alpha\beta}$ up to linear terms in B . This method still requires analytic continuation, but avoids measurements in a finite field. However, in this approach one must evaluate a correlation function of higher order fermion operators (six fermions in the Hubbard model), which can increase error propagation. In addition, by introducing an extra imaginary time and an extra space index, the simulation becomes computationally more expensive. We provide additional detail in Appendix A.

In Ref. [25], another route was laid for studying R_H numerically. As an application of the recursion method [31, 32], this technique expands the Kubo formula of dc Hall conductivity in a Liouvillian representation into terms determined by magnetization matrix elements and Liouvillian matrix elements (or recurrences) [33] in a Krylov basis. By expanding $R_H = \sum_k R_H^{(k)}$, where $R_H^{(k)}$ consist of thermodynamic susceptibilities, the expansion avoids the need for analytic continuation [25, 34]. We refer to this method as the recurrent expansion. One drawback of this method is that the expansion is only conditionally convergent and its truncation error can be hard to estimate for strongly interacting systems.

In previous work [15], we investigated the dc Hall coefficient R_H of the Hubbard model using DQMC to evaluate the leading order of the recurrent expansion $R_H^{(0)}$, showing a strong temperature dependence - increasing with decreasing temperature - mimicking the behavior seen in cuprates [16]. Despite the strong temperature dependence deviating from Fermi liquid behavior, the sign of R_H displayed a surprisingly close relationship with the Fermi surface topology, which has been usually understood as a feature of free electrons. As the interaction increases or the doping decreases towards half filling, R_H changes sign concomitant to changes in Fermi surface topology. We argued that the ‘‘Hall coefficient sign – Fermi surface topology’’ correspondence may apply even for very strong interactions and low doping, in close proximity to a Mott insulator.

Higher-order corrections in the recurrent expansion of R_H [25, 34] could be large enough to qualitatively change this behavior. In the expansion described in Refs. [25, 34], the higher order k^{th} magnetization matrix elements and recurrences are constructed from correlators containing operators proportional to $d^k J_\alpha / dt^k$, where J_α is the current operator along the $\alpha = x$ or y direction. $d^k J_\alpha / dt^k$ may produce terms that include a number of fermion operators, which makes these higher order recurrences more computationally expensive to measure in comparison to $R_H^{(0)}$.

Since the convergence rate of the recurrent expansion is hard to determine away from weak coupling, and higher order corrections are expensive to calculate, we consider the two approaches mentioned previously, which focus directly on the field response of $\chi_{\alpha\beta}$. As exact expressions measured in a well-controlled algorithm, they can be compared with our result for $R_H^{(0)}$ [15]. The imaginary time dependence of $\chi_{\alpha\beta}$ also contains real-time dynamic information about the conductivities.

In this work, we use numerically exact DQMC simulations to evaluate the dc Hall coefficient R_H in the weak-field limit using multiple methods:

- Recurrent Expansion – leading order $R_H^{(0)}$ in terms of thermodynamic susceptibilities [15, 25, 34],
- Zero Field (ZF) – the three-current linear-response of the off-diagonal part of the correlator $\chi_{\alpha\beta}$ to first order in the magnetic field, $\chi_{\alpha\beta}^{\text{ZF}}$.
- Finite Field (FF) – directly evaluating $\chi_{\alpha\beta}$ for a gauge invariant Hamiltonian in weak finite-fields on a finite-size lattice [35], $\chi_{\alpha\beta}^{\text{FF}}$.

We compare results from the latter two methods directly in imaginary time, finding a high degree of consistency, demonstrating that the DQMC algorithm is well-equipped to handle orbital effects of magnetic fields. To avoid the caveats of analytic continuation, we estimate various proxies for R_H from the three-current correlation function. We find reasonable consistency with previous results for $R_H^{(0)}$ [15]. These findings reaffirm the correspondence between the sign structure exhibited by $R_H^{(0)}$ and the topology of the underlying Fermi surface, even in the limit of strong correlations that lack well-formed quasiparticles. In addition, we find that R_H varies more slowly in Matsubara frequency than the individual longitudinal or transverse conductivities. We speculate that the cancellation of strong Matsubara frequency dependence of the individual conductivities also may be related to the observed correspondence between R_H and the Fermi surface topology [15].

The remainder of this paper is organized as follows. In section II, we discuss the inclusion of orbital magnetic fields into the DQMC algorithm, and provide an expression of the zero-field linear response χ_{xy}^{ZF} and show the comparisons between the ZF and FF results in imaginary time. In section III we construct proxies for esti-

mating the Hall coefficient from χ_{xy}^{ZF} and χ_{xx} (taken as the ZF longitudinal response) and discuss the comparisons between them. We close with a discussion of our results and the challenges that remain for an evaluation of the full frequency dependence of the conductivities in the Hubbard model in a magnetic field.

II. CURRENT-CURRENT CORRELATION FUNCTIONS IN THE PRESENCE OF A MAGNETIC FIELD

In this section, we first discuss the inclusion of magnetic fields into the Hubbard model and derive an expression for the off-diagonal component of the current-current correlation function, to linear order in the magnetic field. We compare this directly to the current-current correlation measured under the lowest nonzero allowed field in imaginary time.

Here and throughout the paper, we have neglected Zeeman coupling of applied magnetic fields to spins and focus solely on the orbital contributions relevant for the Hall conductivity. The Hamiltonian of the Hubbard model in the presence of an orbital magnetic field is

$$H(B) = -t \sum_{\langle \mathbf{r}_1, \mathbf{r}_2 \rangle, \sigma} c_{\mathbf{r}_1, \sigma}^\dagger c_{\mathbf{r}_2, \sigma} e^{i\theta_{\mathbf{r}_1, \mathbf{r}_2}} - \mu \sum_{\mathbf{r}, \sigma} n_{\mathbf{r}, \sigma} + U \sum_{\mathbf{r}} n_{\mathbf{r}, \uparrow} n_{\mathbf{r}, \downarrow}, \quad (1)$$

where t is nearest-neighbor hopping energy, μ is the chemical potential, U is the on-site repulsive interaction, $c_{\mathbf{r}, \sigma}^\dagger$ ($c_{\mathbf{r}, \sigma}$) is the creation (annihilation) operator for an electron at position \mathbf{r} with spin σ , and $n_{\mathbf{r}, \sigma} \equiv c_{\mathbf{r}, \sigma}^\dagger c_{\mathbf{r}, \sigma}$ is the number operator, with real-space lattice position \mathbf{r} given by $\mathbf{r} = x\mathbf{e}_x + y\mathbf{e}_y$, where \mathbf{e}_x and \mathbf{e}_y are unit vectors and the lattice constant is set to 1. The model is placed on a square lattice and we use periodic boundary conditions such that $c_{r+L_x\mathbf{e}_x} \equiv c_{r+L_y\mathbf{e}_y} \equiv c_r$, unless otherwise specified, where L_x and L_y are the linear size of the system in the x and y directions, respectively. Here, $\theta_{\mathbf{r}_1, \mathbf{r}_2} = \int_{\mathbf{r}_1}^{\mathbf{r}_2} \mathbf{e} \cdot \mathbf{A}(\mathbf{r}) \cdot d\mathbf{r}$ is the Peierls phase and \mathbf{A} is the vector potential, and this Peierls phase integral is calculated using the shortest straight line path. Finally, the current density operator [36] is given by

$$J_\alpha(\mathbf{r}; B) = -iet \sum_{\sigma} c_{\mathbf{r}+\mathbf{e}_\alpha, \sigma}^\dagger c_{\mathbf{r}, \sigma} e^{i\theta_{\mathbf{r}+\mathbf{e}_\alpha, \mathbf{r}}} + \text{h.c.} \quad (2)$$

To circumvent the problem that the magnitude of a uniform field is limited to integer multiples of the flux quantum $\Phi_0 = 2\pi/e$ on a torus, we take the magnetic field to have a finite wavevector $B(\mathbf{r}) = B \cos(qy)$ with $q = 2\pi/L_y$ in finding the zero-field linear response expression. With this choice, the field magnitude B can be arbitrarily small while maintaining periodic boundary conditions. We have verified that for the systems sizes investigated here, the value of q does not affect the overall results (See Appendix C).

Expanding the current-current correlation function to first order in B yields,

$$\begin{aligned} \chi_{xy}(\mathbf{r}, \tau) &\equiv - \sum_{\mathbf{r}''} \langle T_\tau J_x(\mathbf{r}, \tau; B) J_y(\mathbf{r}'', 0; B) \rangle_B / B \\ &= - \int_0^\beta d\tau' \sum_{\mathbf{r}' \mathbf{r}''} A_x(\mathbf{r}') \langle T_\tau J_x(\mathbf{r}, \tau) J_x(\mathbf{r}', \tau') J_y(\mathbf{r}'', 0) \rangle / B + O(B), \end{aligned} \quad (3)$$

where T_τ is the imaginary time ordering operator, $\beta = 1/k_B T$, T is the temperature, and we use the gauge where $\mathbf{A}(\mathbf{r}) = -(B \sin(qy)/q) \mathbf{e}_x$. Here, $\langle \dots \rangle_B$ denotes the expectation value taken with the full Hamiltonian, while $\langle \dots \rangle$ is taken with the $B = 0$ Hamiltonian. [37]

Next, by making use of translation and reflection symmetries of the unperturbed Hamiltonian, we find

$$\chi_{xy}(\mathbf{r}, \tau) = B(\mathbf{r}) \chi_{xy}^{\text{ZF}} / B + O(B), \quad (4)$$

where

$$\begin{aligned} \chi_{xy}^{\text{ZF}}(\tau) &= \int_0^\beta d\tau' \sum_{\mathbf{r}' \mathbf{r}''} \frac{\sin(q(y' - y''))}{q} \\ &\quad \times \langle T_\tau J_x(\mathbf{r}'', \tau) J_x(\mathbf{r}', \tau') J_y(\mathbf{0}, 0) \rangle \end{aligned} \quad (5)$$

is the zero-field linear response, which we evaluate using DQMC simulations. We note in passing that a similar expression was derived for the case of a continuum model in the limit $q \rightarrow 0$ [38–40].

In addition to χ_{xy}^{ZF} , we also consider the current-current correlation function in a uniform magnetic field. As discussed above, the smallest uniform magnetic field that can be applied corresponds to a single flux quantum through the system $B = \Phi_0/V$, where $V = L_x L_y$ is the area of the system. We use the gauge $\mathbf{A} = B(-y\mathbf{e}_x + x\mathbf{e}_y)/2$ and the corresponding modified periodic boundary conditions

$$\begin{aligned} c_{\mathbf{r}+L_x\mathbf{e}_x} &\equiv c_{\mathbf{r}} e^{-i e B L_x y / 2}, \\ c_{\mathbf{r}+L_y\mathbf{e}_y} &\equiv c_{\mathbf{r}} e^{i e B L_y x / 2}, \end{aligned}$$

following Ref. [41]. We then define the finite-field current-current correlation function as

$$\chi_{xy}^{\text{FF}}(\tau) = \frac{-1}{VB} \sum_{\mathbf{r}, \mathbf{r}'} \langle T_\tau J_x(\mathbf{r}, \tau; B) J_y(\mathbf{r}', 0; B) \rangle_B. \quad (6)$$

We evaluate χ_{xy}^{FF} by performing a separate set of simulations in the presence of a magnetic field, and compare with χ_{xy}^{ZF} . The two expressions are expected to agree in the thermodynamic limit. Technical details of simulations can be found in Appendix A.

While $\hbar = 1$ for convenience, in natural units the unit of conductivity σ is e^2/\hbar and the unit of magnetic field strength B is $\hbar/(ea^2) = \hbar/e$ for lattice constant $a = 1$. Therefore, our unit for R_H is e^{-1} .

Results for $\chi_{xy}^{\text{ZF}}(\tau)$ and $\chi_{xy}^{\text{FF}}(\tau)$ (both purely imaginary) plotted against imaginary time are shown in Fig. 1. Generally, the transverse conductivity is reduced for large

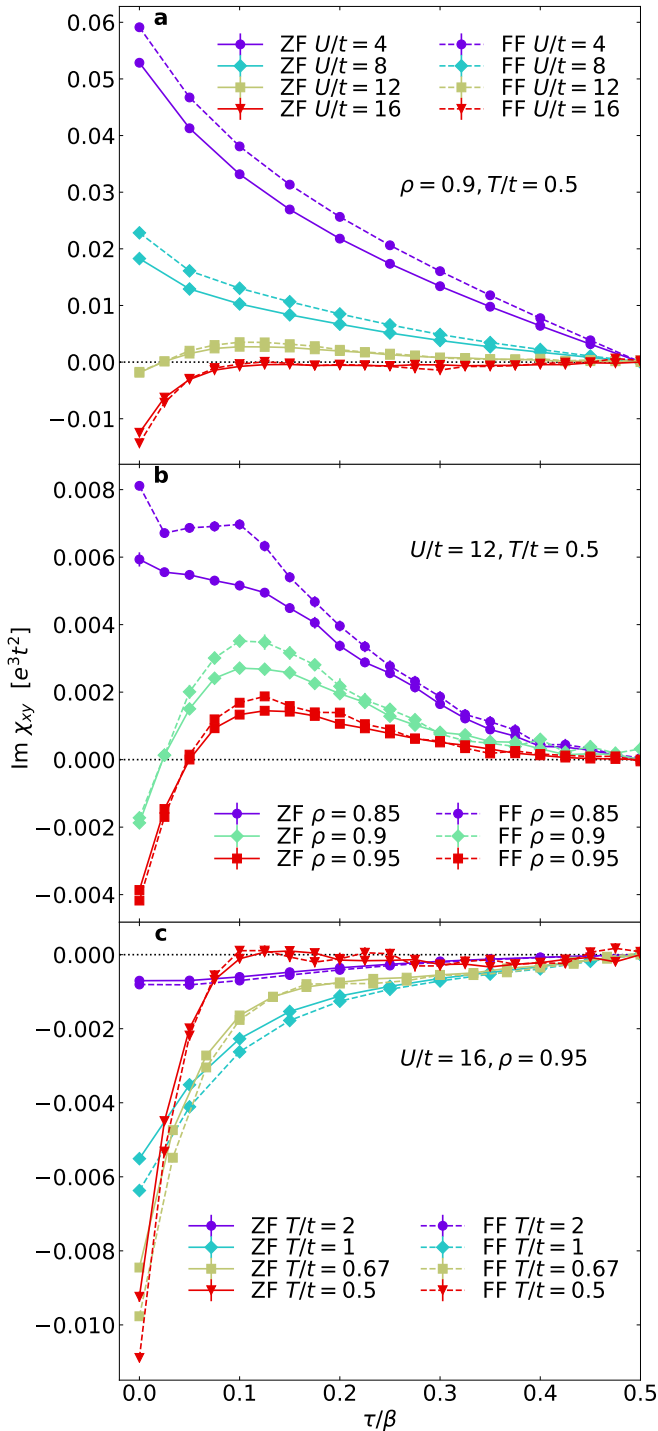


FIG. 1. Comparisons between zero-field (ZF, solid lines) $\text{Im} \chi_{xy}^{\text{ZF}}$ (Eq. 3) and finite-field (FF, dashed lines) $\text{Im} \chi_{xy}^{\text{FF}}(\tau)$ (Eq. 6) in imaginary time for calculations on a 6×6 lattice. **a** A comparison at fixed filling ($\rho = 0.9$) and temperature ($T/t = 0.5$) for interaction strengths $U/t = 4 - 16$. **b** A comparison for fixed $U/t = 12$ and $T/t = 0.5$ for fillings $\rho = 0.85 - 0.95$. **c** A comparison for fixed $U/t = 16$ and $\rho = 0.95$ for temperatures $T/t = 0.5 - 2$. The ZF and FF values have the same units $-e^3 t^2$. Error bars represent ± 1 standard error of the mean, determined by jackknife resampling [42].

U , Fig. 1a, and as half filling is approached, Fig. 1b, as expected when charge fluctuations are suppressed at large U and particle-hole symmetry is restored at half-filling. The zero field (ZF) result $\chi_{xy}^{\text{ZF}}(\tau)$ also qualitatively matches the finite field (FF) result χ_{xy}^{FF} . The significant features, including doping dependence, temperature dependence, and imaginary time dependence, agree quite well between ZF and FF, which implies that when converted to $\sigma_{xy}(\omega)/B$, the two methods should also produce similar frequency dependent features. We verified that the small discrepancies between ZF and FF results are reduced for larger lattice sizes, as shown in Fig. 6 of Appendix C. We henceforth suppress the labels FF and ZF from $\chi_{xy}^{\text{ZF/FF}}$ unless it is needed.

We observe that $\partial_\tau \text{Im} \chi_{xy}$ at $\tau = \beta/2$ tends to increase with increasing U or decreasing doping, and may even change sign for certain parameters (see Fig. 5 in the Appendix for more details). As the off-diagonal conductivity is related to χ_{xy} by (Appendix B)

$$\begin{aligned} \chi_{xy}(\tau) &= i \int_0^\infty \frac{d\omega}{\pi} \frac{\omega^2 \sinh[\omega(\tau - \beta/2)]}{\sinh(\omega\beta/2)} \frac{\text{Im} \sigma_{xy}(\omega)}{\omega B} \\ &\equiv i \int_0^\infty d\omega K(\tau, \omega) \frac{\text{Im} \sigma_{xy}(\omega)}{\omega B}, \end{aligned} \quad (7)$$

by symmetry, $\chi_{xy}(\tau = \beta/2) = 0$. For $U = 0$, in the thermodynamic limit, $\partial_\tau \chi_{xy}$ does not depend on τ . In this case, Eq. 7 leads to $\omega \text{Im} \sigma_{xy}(\omega) \propto \delta(\omega)$, as expected for infinite lifetime quasiparticles in the non-interacting limit. In Fig. 1a-b, we see that χ_{xy} measured under the weakest interaction strength ($U/t = 4$) and lowest filling ($\rho = 0.85$) shows similar τ behavior to that expected for $U = 0$, and shows strong deviations with increasing U or as the system approaches a Mott insulator at half filling. The large curvature of $\text{Im} \chi_{xy}(\tau)$ at small τ reflects the features of $\sigma_{xy}(\omega)$ at $\omega \sim U$ due to transitions to the upper Hubbard band. This becomes more pronounced at low temperatures and higher U as evident in Fig. 1c.

III. PROXIES

We wish to obtain the zero frequency limit of the transverse conductivity from the imaginary time result shown in Fig. 1. Normally, this procedure for the longitudinal conductivity σ_{xx} involves inverting

$$\chi_{xx}(\tau) = - \int_0^\infty \frac{d\omega}{\pi} \frac{\omega \cosh[\omega(\tau - \beta/2)]}{\sinh(\omega\beta/2)} \text{Re} \sigma_{xx}(\omega), \quad (8)$$

where $\chi_{xx}(\tau) \equiv - \sum_{\mathbf{r}', \mathbf{r}} \langle J_x(\mathbf{r}, \tau), J_x(\mathbf{r}', 0) \rangle / V$. Since $\text{Re} \sigma_{xx}(\omega)$ is positive definite, maximum entropy techniques (MEM) [29, 30] may be employed to obtain $\sigma_{xx}(\omega)$ from $\chi_{xx}(\tau)$. However this is not the case for the imaginary part of the transverse frequency dependent conductivity $\text{Im} \sigma_{xy}$, and as a result MEM techniques encounter difficulties. This can be seen in Fig. 1 wherein $\text{Im} \chi_{xy}(\tau)$ can change sign in the range $[0, \beta/2)$, while the kernel $K(\tau, \omega)$ in Eq. 7 does not change sign.

In addition, the six-fermion correlator in χ_{xy}^{ZF} is computationally expensive to measure and suffers from large numerical errors. Therefore, in this section, to compare our χ_{xy}^{ZF} result obtained from Eq. 5, with $R_H^{(0)}$ obtained in Ref. [15], we construct proxies for dc R_H using χ_{xy}^{ZF} , and compare these proxies to $R_H^{(0)}$.

We consider two types of proxies that we derive and discuss below:

- D type – stemming from an analogy to Drude theory: expressed as

$$R_H^{\text{D}} = -iT \frac{(\partial_\tau \chi_{xy}^{\text{ZF}})(\tau = \beta/2)}{[\chi_{xx}(\tau = \beta/2)]^2}, \quad (9)$$

which is obtained by inserting the Drude formulas

$$\sigma_{xy}|_{B=0} = \Omega_{xy} \frac{1}{(\gamma - i\omega)^2}, \quad (10)$$

$$\sigma_{xx}|_{B=0} = \Omega_{xx} \frac{1}{\gamma - i\omega} \quad (11)$$

into Eq. 7 and 8 and taking the limit $\gamma \rightarrow 0$, where γ is the scattering rate. Another candidate proxy D_γ is constructed by assuming γ to be non-zero and fitting χ_{xx} and χ_{xy}^{ZF} using Eqs. 7, 8, 10, and 11. Results of proxies D and D_γ are shown in Fig. 2a-c.

- M type – determined by extracting the zero Matsubara frequency limit of:

$$R_H^{\text{M1}}(i\omega_n) = \frac{\chi_{xy}^{\text{ZF}}(i\omega_n)\omega_n}{[\chi_{xx}(i\omega_n) - \chi_{xx}(i\omega = 0)]^2}, \quad (12)$$

where $\chi_{\alpha\beta}(i\omega_n)$ in Matsubara frequency is defined as the Fourier transform of the imaginary time data, given by $\chi_{\alpha\beta}(i\omega_n) = \int_0^\beta d\tau e^{i\omega_n\tau} \chi_{\alpha\beta}(\tau)$. Here we utilize a cubic spline interpolant. Another candidate proxy M2 is defined as

$$R_H^{\text{M2}} = \frac{\chi_{xy}^{\text{ZF}}(i\omega_1)\pi^2}{\omega_1 [\chi_{xx}(\tau = \beta/2)]^2 \beta^4}, \quad (13)$$

where $\omega_1 = 2\pi/\beta$, the smallest nonzero Matsubara frequency. Results of proxies M1 and M2 are shown in Fig. 2d-f.

Figure 2 displays comparisons between $R_H^{(0)}$ and the proxies D, D_γ , M1, M2, and generally shows that D, D_γ , and M1 closely match $R_H^{(0)}$ from previous work [15], at least within a factor of order unity. Proxy M2, on the other hand, consistently produces results that are much smaller (about 1/4 of M1) in magnitude. Calculation details of these proxies are in Appendix D.

For a Fermi liquid with a momentum-independent scattering rate γ , theoretical work [8, 43–46] has demonstrated a Drude-like ω dependence of the conductivities in Eq. 10 and 11 for $\omega \lesssim \gamma$. Therefore, we expect proxy

D to be in good agreement with the true R_H for a Fermi liquid where the scattering is isotropic and weak. Details of the derivation of Eq. 9 can be found in Appendix D.

Figures 2a-c show proxy D. For weak U ($\sim 4t$), or higher doping ($\rho \leq 0.9$), proxy D fits previous results of $R_H^{(0)}$ very well, as expected for a normal metal. In these parameter regimes, results for either proxy D or $R_H^{(0)}$ should be deemed reliable. Approaching the Mott insulator where one should not expect Drude theory to apply, proxy D unsurprisingly deviates from $R_H^{(0)}$.

Proxy D_γ assumes γ to be non-zero and finite. As shown in Fig. 2a-c, the results for proxy D_γ are largely the same as those of proxy D, implying that under the assumptions of Drude theory, our estimation of R_H is not sensitive to changes in relaxation rate. As we can see from Eq. 10 and Eq. 11, any direct effect of γ cancels out in R_H .

There are some limitations for D-type proxies. Conductivities can deviate significantly from Drude theory for strongly interacting systems, leaving the approximate R_H far from the true results. In addition, from solely Eq. 7 and 10, one can never obtain a $\text{Im} \chi_{xy}(\tau)$ that changes sign as a function of τ in the range $\tau \in [0, \beta/2)$, which is an important feature in our $\text{Im} \chi_{xy}(\tau)$ data due to interaction effects.

Now we switch to the M type proxies. Proxy M1 using Eq. 12 is exact for dc R_H in the zero-temperature limit $T \ll \Lambda$ ($\omega_n \ll \Lambda$), where Λ is defined as the scale on which $\chi_{\alpha\beta}$ begins to deviate from its low-frequency behavior. This is because

$$\frac{\sigma_{xy}(i\omega)}{B} = \frac{\chi_{xy}(i\omega)}{\omega}, \quad (14)$$

$$\sigma_{xx}(i\omega) = \frac{\chi_{xx}(i\omega) - \chi_{xx}(i\omega = 0)}{\omega} \quad (15)$$

(see Appendix B and [21]).

Proxy M2 approximates $\sigma_{xx}(\omega = 0)$ with

$$-\frac{\beta^2}{\pi} \chi_{xx}(\tau = \beta/2) \quad (16)$$

and uses $\omega = \omega_1$ to estimate Eq. 14 at $\omega = 0$. Equation 16 is also exact at $T \ll \Lambda$, and is often used as a proxy for σ_{xx} in other work [10].

Figures 2d-f show proxies M1 and M2. Values of M1 are overall close to those for both proxy D and D_γ , even for strong interactions up to $U = 16t$. Indeed generally, as long as the rapidly varying components in $\sigma_{xy}(i\omega)$ and $\sigma_{xx}(i\omega)$ cancel out in $R_H^{\text{M1}}(i\omega)$, proxy M1 is very accurate regardless of the explicit form of frequency dependence of the conductivities. In other words, proxy M1 only requires the ratio of the conductivities, $R_H^{\text{M1}}(i\omega_n)$, to vary slowly with ω_n , as we show in Fig. 3, where we plot $R_H^{\text{M1}}(i\omega_n)$ against n (similar to Ref. [21]). Proxy M2 is not able to make use of cancellation between the transverse and longitudinal conductivities, so it still requires $T \ll \Lambda$ for both conductivity components. The difference between values of M1 and M2 in our simulations

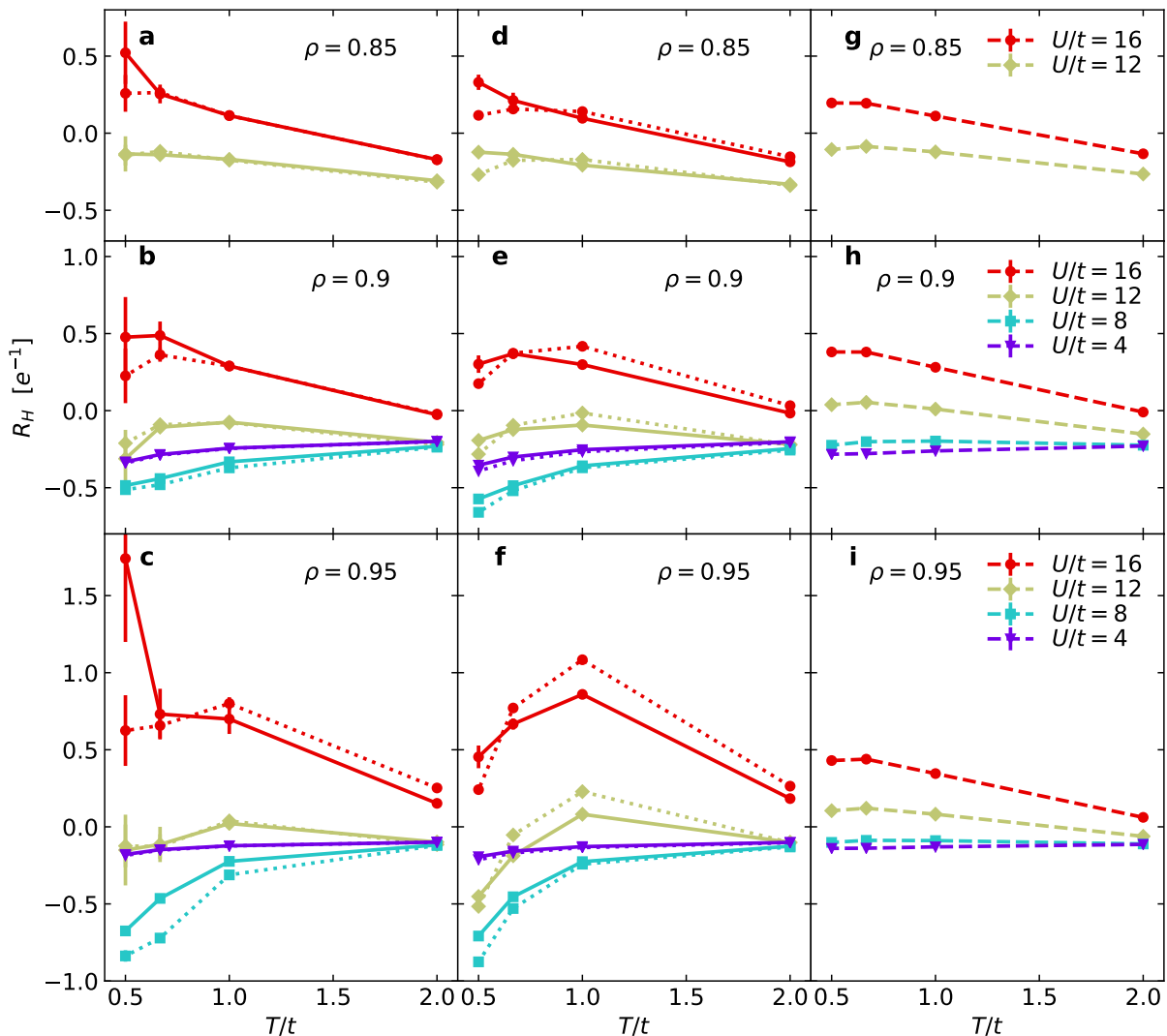


FIG. 2. dc Hall coefficient as determined from the proxies D, D_γ , M1, and M2, as well as how these proxies compare to $R_H^{(0)}$. M2 has been multiplied by a factor of 4 to demonstrate that it has similar temperature and doping dependence, as well as sign change structure, as other proxies, but with a reduced magnitude. Panels in the same row share the same legend. For all proxies, $\chi_{xy}^{ZF}(\tau)$ is measured on a 6×6 lattice, and $\chi_{xx}(\tau)$ is measured on a 8×8 lattice. Pairs of a dotted and solid lines in panels **a-f** share the same parameters. **a-c** Proxy D (solid) and proxy D_γ (dotted). **d-f** Proxy M1 (solid) and proxy M2 ($\times 4$, dotted). **g-i** Dashed lines are $R_H^{(0)}$, defined by the leading order term in the expression for R_H in Refs. [25] and [34], constructed from thermodynamic susceptibilities. These are evaluated on 8×8 lattices. Error bars represent ± 1 standard error determined by jackknife resampling.

indicates that $\Lambda \lesssim T$, so that $\sigma_{xy}(i\omega)$ and $\sigma_{xx}(i\omega)$ vary significantly within the scale set by the smallest non-zero Matsubara frequency ω_1 .

Considering that D and M type proxies have different assumptions and approach R_H from quite different aspects, it is remarkable that D, D_γ , and M1 are overall comparable to each other. Even more remarkably, all the proxies compare particularly well to the sign changing structure to $R_H^{(0)}$. Also considering the previous comparison of ZF results with those of FF in Sec. II, we conclude that the previous method we used to calculate $R_H^{(0)}$ [15] as an approximation for R_H is reliable for large U , de-

spite our neglect of higher order corrections. As we have shown in this section, the proxies constructed using χ_{xy}^{ZF} and χ_{xx} are also a useful approximation when direct analytic continuation to find $\sigma_{xy}(\omega)$ is challenging.

We remark that within the temperatures accessible for DQMC simulation, our R_H results do not show a strong doping dependence away from half-filling, specifically in the region around 20% hole doping as referenced in cuprate experiments [47–49].

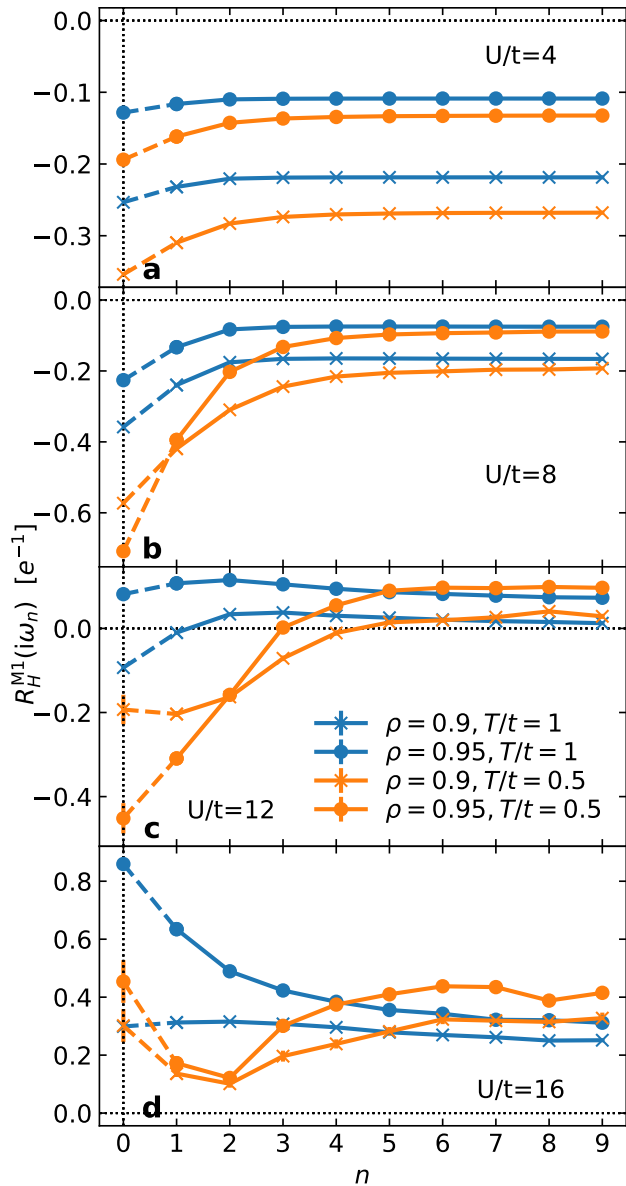


FIG. 3. $R_H^{M1}(i\omega_n)$ in Matsubara frequency. Data are shown for $U/t = 4 - 16$ for panels **a-d**, respectively, with $\rho = 0.9$ and 0.95 and temperature $T/t = 0.5$ and 1 . The data points at $\omega_n = 0$ correspond to proxy M1 shown in Fig. 2. χ_{xy}^{ZF} was calculated on a 6×6 lattice, while χ_{xx} was calculated on an 8×8 lattice. Error bars for $n > 0$ are smaller than the points.

IV. DISCUSSION

Through a consideration of various methods to evaluate the Hall coefficient, we have demonstrated agreement between the sign change structures of χ_{xy}^{ZF} , χ_{xy}^{FF} , and $R_H^{(0)}$, supporting prior claims that the sign of the dc Hall coefficient has a close relationship to the Fermi surface topology in the strongly correlated zero-field Hubbard model [15]. The rough agreement between proxy D, D_γ , M1 and $R_H^{(0)}$, as well as the significantly dif-

ferent result of proxy M2, suggests that making use of cancellation between transport quantities may simplify evaluations of difficult multifermion correlation functions such as the Hall coefficient and allow us to construct a good description of transport without quasiparticles. The following facts lend support to our idea. While longitudinal resistivity in the Hubbard model shows typical non-Fermi liquid behavior [10], R_H shows relatively flat ω_n -dependence in Fig. 3. In this work, proxy D and D_γ provide similar results. This likely results from our assumption that γ is the same for the two conductivities, leading indirectly to simplifications that allow D_γ to mimic D due to apparent cancellation of lifetime effects. In constructing proxy M2, there are no such cancellations, and the proxy is fragile and easily fails. Finally, Refs. [25] and [34] showed how ratios of conductivities like the Hall coefficient or thermal Hall coefficient reduce to expressions constructed from simple thermodynamic susceptibilities. It is an open and intriguing question whether a Fermi-liquid like correspondence between Fermi surface topology and R_H in Ref. [15] is due to such cancellations between conductivities, rather than necessarily Fermi-liquid-like ω -dependence of each conductivity.

It remains a challenge to perform analytic continuation directly from Matsubara frequencies or imaginary time data. A promising approach would be to use techniques designed to treat non-positive-definite spectra [50, 51], or other methods of analytic continuation [52–55]. If a reliable method of analytic continuation can be found, then our evaluation of the exact three-current linear-response χ_{xy}^{ZF} through the numerically exact and unbiased DQMC algorithm will allow us to find the exact $\sigma_{xy}(\omega)$ spectra for all frequencies for the Hubbard model. Even in the absence of reliable analytic continuation methods, our χ_{xy}^{ZF} results will still be a benchmark for any theory that proposes a frequency dependence of σ_{xy} for the strongly correlated Hubbard model or similar models.

The data and analysis routines (Jupyter/Python) needed to reproduce the figures can be found at <https://doi.org/10.5281/zenodo.4569163>.

ACKNOWLEDGMENTS

We acknowledge helpful discussions with S. Kivelson, S. Lederer, A. Auerbach and I. Khait. *Funding:* This work was supported by the U.S. Department of Energy (DOE), Office of Basic Energy Sciences, Division of Materials Sciences and Engineering. EWH was supported by the Gordon and Betty Moore Foundation EPiQS Initiative through the grants GBMF 4305 and GBMF 8691. YS was supported by the Gordon and Betty Moore Foundation's EPiQS Initiative through grants GBMF 4302 and GBMF 8686. Computational work was performed on the Sherlock cluster at Stanford University and on resources of the National Energy Research Scientific Computing Center, supported by the U.S. DOE, Office of Sci-

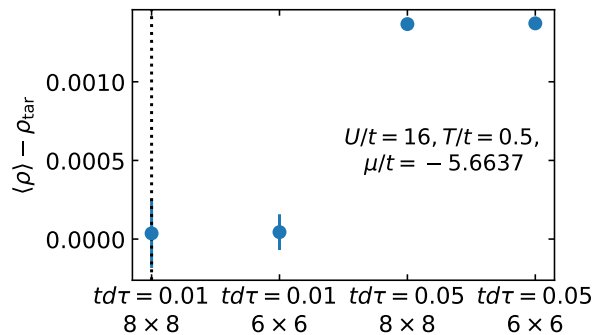


FIG. 4. An example of the error in density associated with μ for the ZF case, shown as the difference between the measured density $\langle \rho \rangle$ and the target density ρ_{tar} , for different $d\tau$ and lattice sizes. The parameters $U/t = 16$, temperature $T/t = 0.5$ and $\rho_{\text{tar}} = 0.9$ are selected, as $U/t = 16$ is the largest interaction strength that we consider, with the most severe Trotter error. The dotted line indicates the parameters used in tuning μ for the target ρ_{tar} (The largest cluster and smallest $d\tau$).

ence, under Contract no. DE-AC02-05CH11231.

Appendix A: simulation details

We use DQMC simulations to measure $\chi_{xy}^{\text{ZF}}(\tau)$ for the Hubbard model in Eq. 1 without B and $\chi_{xy}^{\text{FF}}(\tau)$ under $eB = 2\pi/V$, respectively, on a 2D square lattice with the corresponding periodic boundary conditions [41]. Strategies for evaluating Green's functions in this work are the same as those of Ref. [10].

We can write down an alternate expression for χ_{xy}^{ZF} :

$$\chi_{xy}^{\text{ZF}}(\tau) = \int_0^\beta d\tau' \sum_{\mathbf{r}'\mathbf{r}''} \frac{\sin(q(x' - x''))}{q} \times \langle T_\tau J_y(\mathbf{r}'', \tau) J_y(\mathbf{r}', \tau') J_x(\mathbf{0}, 0) \rangle. \quad (\text{A1})$$

Because of C_4 symmetry, we confirm that χ_{xy}^{ZF} given in Eqs. 5 and A1 give identical results and report the average of the two quantities to reduce sampling errors and improve statistical measurements. Similarly, since $\chi_{xy}^{\text{FF}}(\tau) = -\chi_{yx}^{\text{FF}}(\tau)$, we measure and report $(\chi_{xy}^{\text{FF}} - \chi_{yx}^{\text{FF}})/2$.

In our simulations for χ_{xy}^{ZF} , we measure $\langle T_\tau \mathbf{J}(\tau) \mathbf{J}(\tau') \mathbf{J}(0) \rangle$ at discretized τ' values. The integral over τ' is computed by finding two cubic spline interpolants using data points in the ranges $\tau' \in [0, \tau]$ and $\tau' \in [\tau, \beta]$ respectively (here $\langle T_\tau \mathbf{J}(\tau) \mathbf{J}(\tau') \mathbf{J}(0) \rangle$ is discontinuous at $\tau' = \tau$ due to time ordering) and then integrating the interpolants.

To tune the chemical potential μ for a specific target filling level ρ_{tar} at a specific temperature, we use DQMC to calculate $\langle \rho \rangle$ for a range of chemical potentials μ (at $0.05t$ intervals for ZF case and $0.1t$ intervals for FF case) and obtain the best μ by linear interpolation of the $\langle \rho \rangle$ versus chemical potential curve. In the ZF case, μ is

tuned on a 8×8 lattice and the same μ is used for both 8×8 and 6×6 lattice sizes. In the FF case, μ tuning for 6×6 and 8×8 lattices are done separately, although in practice, the optimal μ is almost identical for the two lattice sizes. For our parameters, we can obtain $\langle \rho \rangle$ to within a tolerance of $O(10^{-3})$ of the target density ρ_{tar} (written as ρ throughout this work). An example of this tolerance in the ZF case is shown in Fig. 4. Including the effects of the Trotter error, DQMC statistical error, and the density shift between lattice sizes for specific values of μ , our density is accurate to $O(10^{-3})$.

Regarding the Trotter error, we define $d\tau$ as the interval between imaginary time data points. In previous work [15], we set a minimum partition of imaginary time $L = \beta/d\tau = 20$ and a maximum $d\tau = 0.1/t$ for all interactions and temperatures. In this work, for $U/t = 4 - 8$, all ZF calculations (χ_{xy}^{ZF} , χ_{xx} , $R_H^{(0)}$, and $\langle \rho \rangle$) use the same $d\tau$ as in the previous work [15], while FF calculations (χ_{xy}^{FF} and $\langle \rho \rangle$) also have maximum $d\tau = 0.1/t$, but have minimum $L = 10$. So the imaginary time spacing of χ_{xy}^{FF} is larger than χ_{xy}^{ZF} at the highest temperatures, as shown in Fig. 5a-d for $U/t = 4$ and Fig. 6 for $U/t = 8$. For $U/t = 12 - 16$, χ_{xy}^{ZF} , χ_{xx} , χ_{xy}^{FF} , and $R_H^{(0)}$ are all obtained with a maximum $d\tau = 0.05/t$ and minimum $L = 20$, in order to reduce the Trotter error. Measurement of $\langle \rho \rangle$ in tuning of μ is done using a minimum $L = 20$, and a maximum $d\tau = 0.01/t$ (ZF) and $d\tau = 0.02/t$ (FF). In summary, $Ut(d\tau)^2 \leq 0.08$ in this work, comfortably below the conventionally adopted limit $Ut(d\tau)^2 \leq 1/8$. We consider Trotter error to be negligible. The accuracy of our results is affected primarily by the limitations of individual proxies, as discussed in the main text. In addition to Trotter error discussed here, our only other source of systematic error is finite-size effects discussed in Appendix C.

We run up to approximately 600 independently seeded Markov chains for χ_{xy}^{ZF} , about 40 Markov chains for χ_{xx} and $R_H^{(0)}$, and up to 200 Markov chains for χ_{xy}^{FF} . For χ_{xy}^{ZF} , when $U/t = 12 - 16$, each Markov chain has 5×10^5 space-time sweeps, while for $U/t = 4 - 8$, each Markov chain has 10^6 space-time sweeps. χ_{xx} and $R_H^{(0)}$ are measured together and have 10^6 space-time sweeps in each Markov chain. χ_{xy}^{FF} has 5×10^5 to 4×10^6 space-time sweeps in each Markov chain, depending on parameters. For χ_{xy}^{ZF} , χ_{xx} and $R_H^{(0)}$, measurements are performed once every 4 sweeps. For χ_{xy}^{FF} , measurements are performed once every 2 sweeps. Measurements occupy more than 90% of the simulation runtime, meaning χ_{xy}^{ZF} is $O(L_x L_y L)$ more expensive than χ_{xy}^{FF} .

Appendix B: dynamical conductivity

In this section we discuss the relationship between σ_{xy} and χ_{xy} . In the derivations of this section and Appendix D, that relate current-current correlation func-

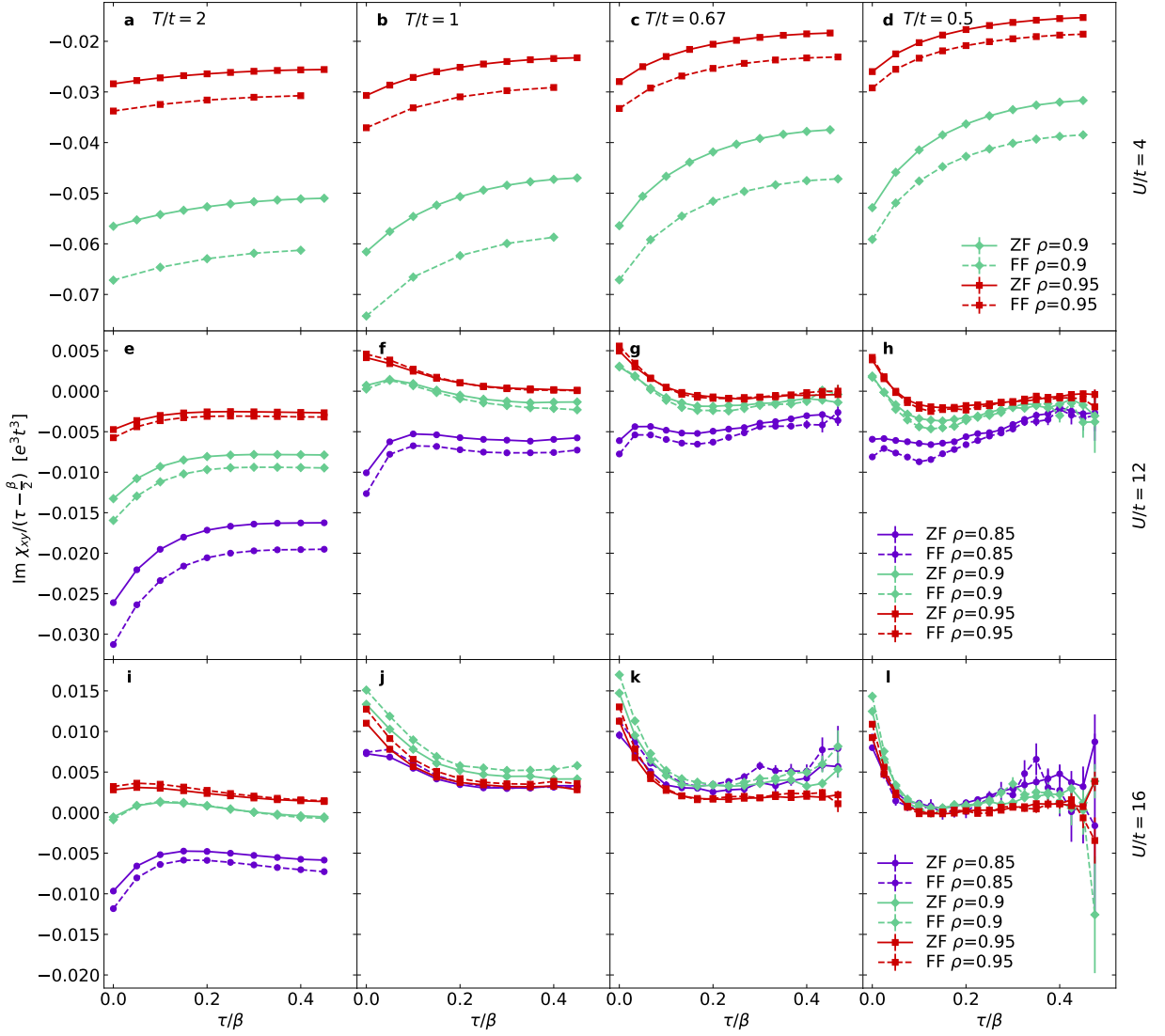


FIG. 5. Supplementary data for Fig. 1 with a direct comparison between the ZF $\text{Im} \chi_{xy}^{\text{ZF}}(\tau)$ and FF $\text{Im} \chi_{xy}^{\text{FF}}(\tau)$. Calculations were performed on 6×6 lattices using the DQMC algorithm. Error bars are ± 1 standard error determined by jackknife resampling. The same color (marker) within each panel represents the same parameters, as referenced in the legends in the final column. Rows have fixed interaction strength U and columns have the fixed temperature T .

tions to conductivities, we assume the thermodynamic limit. In that limit, χ_{xy}^{ZF} is considered to be the linear response to an infinitesimal uniform magnetic field B , *i.e.* $\chi_{xy}^{\text{ZF}} = \lim_{B \rightarrow 0} \chi_{xy}$. On the other hand, in defining χ_{xy}^{ZF} in Eq. 5, we used a finite q and a non-uniform magnetic field to ensure that the expression is well-defined on a finite lattice. This approach is reasonable, as the conductivities obtained in this way converge to their values in the thermodynamic limit as $q \rightarrow 0$.

With the definition of the total current operator $J_\alpha \equiv \sum_{\mathbf{r}} J_\alpha(\mathbf{r})$, the definitions of the $J_x - J_y$ correlators, in imaginary time τ and Matsubara frequency $i\omega_n =$

$i2\pi n/\beta$, are

$$\begin{aligned} \chi_{xy}(\tau) &= -\frac{1}{V} \langle J_x(\tau) J_y \rangle_B / B \\ &= -\frac{1}{ZVB} \sum_{pm} \langle p | J_x | m \rangle \langle m | J_y | p \rangle e^{-\beta E_p} e^{\tau(E_p - E_m)}, \end{aligned} \quad (\text{B1})$$

$$\begin{aligned} \chi_{xy}(i\omega_n) &= \int_0^\beta d\tau e^{i\omega_n \tau} \chi_{xy}(\tau) \\ &= \frac{1}{ZVB} \sum_{pm} \langle p | J_x | m \rangle \langle m | J_y | p \rangle \frac{e^{-\beta E_p} - e^{-\beta E_m}}{i\omega_n + E_p - E_m}. \end{aligned} \quad (\text{B2})$$

In real-time and real-frequency,

$$\begin{aligned}\chi_{xy}^R(t) &= -\frac{i}{VB}\theta(t)\langle [J_x(t), J_y] \rangle_B = \frac{-i\theta(t)}{ZVB}\sum_{pm} \\ \langle p|J_x|m\rangle\langle m|J_y|p\rangle(e^{-\beta E_p} - e^{-\beta E_m})e^{it(E_p - E_m)}, \quad (\text{B3}) \\ \chi_{xy}^R(\omega) &= \int dt e^{i\omega t}\chi_{xy}^R(t) \\ &= \frac{1}{ZVB}\sum_{pm}\langle p|J_x|m\rangle\langle m|J_y|p\rangle\frac{e^{-\beta E_p} - e^{-\beta E_m}}{\omega + E_p - E_m + i0^+}.\end{aligned}\quad (\text{B4})$$

Using $\frac{1}{x+i0^+} = \mathcal{P}\frac{1}{x} - i\pi\delta(x)$, we can break up Eq. B4,

$$\chi_{xy}^R(\omega) = \chi_{xy}^{(1)}(\omega) + i\chi_{xy}^{(2)}(\omega), \quad (\text{B5})$$

$$\begin{aligned}\chi_{xy}^{(1)}(\omega) &= \frac{1}{ZVB}\sum_{pm}\langle p|J_x|m\rangle\langle m|J_y|p\rangle \\ &\quad (e^{-\beta E_p} - e^{-\beta E_m})\mathcal{P}\frac{1}{\omega + E_p - E_m}, \quad (\text{B6})\end{aligned}$$

$$\begin{aligned}\chi_{xy}^{(2)}(\omega) &= \frac{-\pi}{ZVB}\sum_{pm}\langle p|J_x|m\rangle\langle m|J_y|p\rangle \\ &\quad (e^{-\beta E_p} - e^{-\beta E_m})\delta(\omega + E_p - E_m).\end{aligned}\quad (\text{B7})$$

Comparing Eq. B1 and Eq. B7, we see

$$\chi_{xy}(\tau) = \int \frac{d\omega}{\pi} \frac{e^{-\tau\omega}}{1 - e^{-\beta\omega}} \chi_{xy}^{(2)}(\omega). \quad (\text{B8})$$

$\chi_{xy}(\tau)$ is purely imaginary, which one sees as follows: $\langle J_x(\tau)J_y \rangle = \langle J_y(\tau)J_{-x} \rangle = -\langle J_y(\tau)J_x \rangle$. In addition,

$$\begin{aligned}\langle J_y(\tau)J_x \rangle_B &= \frac{1}{Z}\text{Tr}(\exp((\tau - \beta)H)J_y\exp(-\tau H)J_x) \\ &= \frac{1}{Z}\text{Tr}(J_y\exp(-\tau H)J_x\exp((\tau - \beta)H)) = \langle J_x(\tau)J_y \rangle_B^*,\end{aligned}$$

which gives

$$\langle J_x(\tau)J_y \rangle_B^* = -\langle J_x(\tau)J_y \rangle_B. \quad (\text{B9})$$

Since $\chi_{xy}^{(2)}(\omega)$ and $\chi_{xy}^{(1)}(\omega)$ are related by a Kramers-Kronig transform, $\chi_{xy}^{(1)}(\omega)$ is also purely imaginary. So the real part of $\chi_{xy}^R(\omega)$ is $i\chi_{xy}^{(2)}(\omega)$ and the imaginary part of $\chi_{xy}^R(\omega)$ is $\chi_{xy}^{(1)}(\omega)$. The Hall conductivity is (by Kubo formula [36])

$$\frac{\sigma_{xy}(\omega)}{B} = \frac{\chi_{xy}^R(\omega)}{-i\omega}, \quad (\text{B10})$$

$$\frac{\text{Re}\sigma_{xy}(\omega)}{B} = -\frac{\chi_{xy}^{(1)}(\omega)}{i\omega}, \quad (\text{B11})$$

$$\frac{\text{Im}\sigma_{xy}(\omega)}{B} = \frac{i\chi_{xy}^{(2)}(\omega)}{\omega}. \quad (\text{B12})$$

Combining Eq. B12 with Eq. B8, we obtain the useful relation

$$\frac{\chi_{xy}(\tau)}{i} = -\int \frac{d\omega}{\pi} \frac{e^{-\tau\omega}}{1 - e^{-\beta\omega}} \omega \frac{\text{Im}\sigma_{xy}(\omega)}{B}. \quad (\text{B13})$$

The analogous relation we have employed previously to study the diagonal conductivity by measuring $\chi_{xx} \equiv -\langle J_x(\tau)J_x \rangle_B / V$ is [10]

$$\chi_{xx}(\tau) = -\int \frac{d\omega}{\pi} \frac{e^{-\tau\omega}}{1 - e^{-\beta\omega}} \omega \text{Re}\sigma_{xx}(\omega). \quad (\text{B14})$$

$\text{Im}\sigma_{xy}(\omega)/\omega$ and $\text{Re}\sigma_{xx}(\omega)$ are even functions, so we can transform Eq. B13 and Eq. B14 such that

$$\begin{aligned}\frac{\chi_{xy}(\tau)}{i} &= -\int_0^\infty \frac{d\omega}{\pi} \omega^2 \frac{[e^{(\frac{\beta}{2}-\tau)\omega} - e^{-(\frac{\beta}{2}-\tau)\omega}]}{e^{\frac{\beta}{2}\omega} - e^{-\frac{\beta}{2}\omega}} \frac{\text{Im}\sigma_{xy}(\omega)}{\omega B}, \\ \chi_{xx}(\tau) &= -\int_0^\infty \frac{d\omega}{\pi} \omega \frac{[e^{(\frac{\beta}{2}-\tau)\omega} + e^{-(\frac{\beta}{2}-\tau)\omega}]}{e^{\frac{\beta}{2}\omega} - e^{-\frac{\beta}{2}\omega}} \text{Re}\sigma_{xx}(\omega).\end{aligned}$$

These are Eq. 7 and 8 in the main text.

Comparing Eq. B2 and Eq. B4 and considering Eq. B10, we also conclude that

$$\frac{\sigma_{xy}(\omega=0)}{B} = \lim_{\omega \rightarrow 0} \frac{\chi_{xy}(i\omega)}{\omega}. \quad (\text{B15})$$

Appendix C: Finite size effects

A comparison of ZF and FF data obtained using different lattice sizes for $U/t = 8$ and $U/t = 12$ is shown in Fig. 6 and 7, respectively. Fig. 6 reveals that the FF results have smaller finite-size effects than the ZF results. As we have discussed in the main text, we expect the ZF and FF results to be identical in the thermodynamic limit, and that trend is indeed shown in Fig. 6 and Fig. 7.

Appendix D: proxy calculation details

In this section, we start from the Drude formula in Eq. 10 and Eq. 11 and derive proxy D in the limit of weak scattering $\gamma \rightarrow 0$. From Eq. 10 and using $\lim_{\gamma \rightarrow 0} \frac{2\omega^2\gamma}{\pi(\gamma^2 + \omega^2)^2} = \delta(\omega)$, we have

$$\lim_{\gamma \rightarrow 0} \omega \text{Im}\sigma_{xy} = \Omega_{xy}\pi\delta(\omega). \quad (\text{D1})$$

Inserting this into Eq. 7 and calculating the derivative,

$$\begin{aligned}&\lim_{\gamma \rightarrow 0} \left. \frac{\partial}{\partial \tau} \frac{\chi_{xy}(\tau)}{i} \right|_{\tau=\beta/2} \\ &= \int_{-\infty}^\infty \frac{d\omega}{\pi} \frac{\omega}{e^{\beta\omega/2} - e^{-\beta\omega/2}} \omega \lim_{\gamma \rightarrow 0} \text{Im}\sigma_{xy}(\omega)/B \\ &= \frac{1}{\beta B} \Omega_{xy}.\end{aligned}\quad (\text{D2})$$

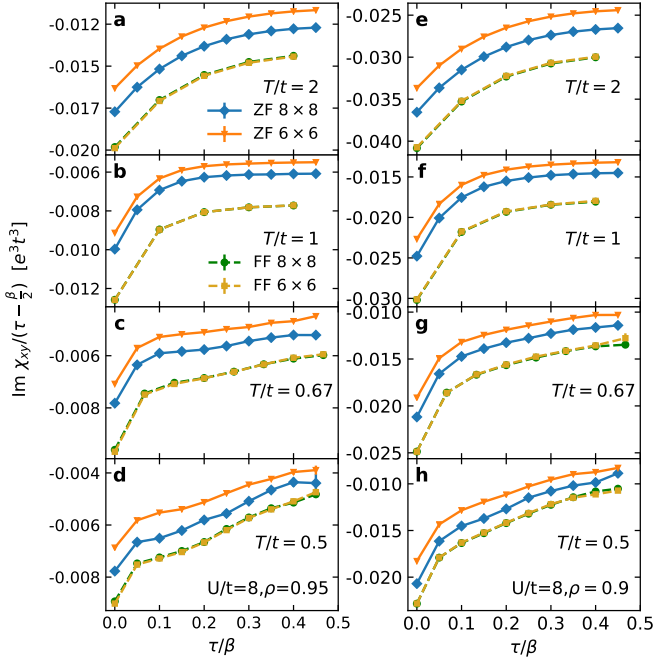


FIG. 6. Finite size analysis for $\text{Im } \chi_{xy}^{\text{ZF}}$ and $\text{Im } \chi_{xy}^{\text{FF}}$ in imaginary time with $U/t = 8$ and $T/t = 0.5 - 2$. $\text{Im } \chi_{xy}^{\text{ZF}}(\tau)$ (solid) and $\text{Im } \chi_{xy}^{\text{FF}}(\tau)$ (dashed) are divided by $\tau - \beta/2$ to accentuate the behavior near $\tau = \beta/2$. **a-d** Filling $\rho = 0.95$ and **e-h** filling $\rho = 0.9$.

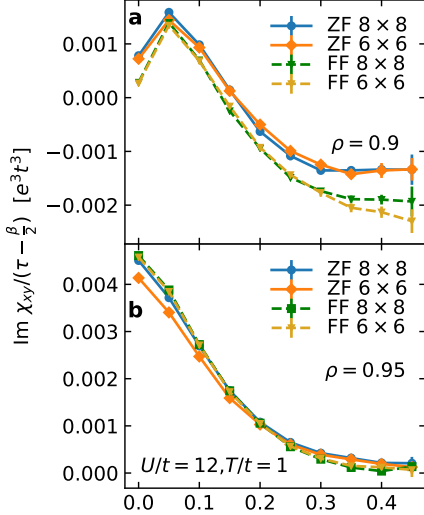


FIG. 7. Finite size analysis for $\text{Im } \chi_{xy}^{\text{ZF}}$ and $\text{Im } \chi_{xy}^{\text{FF}}$ in imaginary time for $U/t = 12$ and $T/t = 1$.

From Eq. 11 and considering $\lim_{\gamma \rightarrow 0} \frac{\gamma}{(\gamma^2 + \omega^2)} = \pi \delta(\omega)$,

$$\lim_{\gamma \rightarrow 0} \text{Re } \sigma_{xx} = \Omega_{xx} \pi \delta(\omega). \quad (\text{D3})$$

Inserting this into Eq. 8 we obtain

$$\begin{aligned} & \lim_{\gamma \rightarrow 0} \chi_{xx}(\tau = \beta/2) \\ &= - \int_{-\infty}^{\infty} \frac{d\omega}{\pi} \frac{1}{e^{\beta\omega/2} - e^{-\beta\omega/2}} \omega \lim_{\gamma \rightarrow 0} \text{Re } \sigma_{xx}(\omega) \\ &= -\frac{1}{\beta} \Omega_{xx}. \end{aligned} \quad (\text{D4})$$

So combining Eqs. 10, 11, D2, and D4, we finally have the expression for the dc Hall coefficient under the assumption that $\gamma \rightarrow 0$,

$$R_H = \left[\frac{\partial}{\partial \tau} \frac{\chi_{xy}(\tau)}{i} \right] \Big|_{\tau=\beta/2} / (\beta [\chi_{xx}(\tau = \beta/2)]^2). \quad (\text{D5})$$

One can test that for the Hubbard model with $U = 0$, $\chi_{xx}(\tau)$ does not vary with τ , and $\partial_{\tau} \chi_{xy}^{\text{ZF}}(\tau)$ does not change with τ in the thermodynamic limit (a/L_x and $a/L_y \ll T/t$). This implies that $\omega \text{Im } \sigma_{xy}(\omega)$ and $\text{Re } \sigma_{xx}(\omega)$ are both $\propto \delta(\omega)$.

For proxy D, we use finite differences to estimate $(\partial_{\tau} \chi_{xy}^{\text{ZF}})(\tau = \beta/2)$. Error bars for proxy D are constructed by error propagation of the standard errors in $(\partial_{\tau} \chi_{xy}^{\text{ZF}})(\tau = \beta/2)$ and $[\chi_{xx}(\tau = \beta/2)]^2$, which themselves are determined by jackknife resampling.

For proxy D $_{\gamma}$, We fit a few values of χ_{xy}^{ZF} and χ_{xx} near $\tau = \beta/2$ to Eq. 10 and 11 through Eq. 7 and 8. In doing so, we assume that the γ s are equal in σ_{xx} and σ_{xy} . We also make use of the fact that values of $\chi_{xx}(\tau)$ and $\chi_{xy}(\tau)$ near $\tau = \beta/2$ are determined more predominantly by the low-frequency Drude-like behavior of conductivities, compared with other τ values. By fitting χ_{xx} we extract γ and Ω_{xx} ; and by fitting χ_{xy}^{ZF} we extract Ω_{xy}/B .

We choose to use σ_{xx} rather than σ_{xy} to find γ for several reasons: DQMC measurements of $\chi_{xx}(\tau)$ have smaller numerical errors than $\chi_{xy}^{\text{ZF}}(\tau)$, and we could use the second derivative of χ_{xx} to estimate γ , but we need to use the third derivative of χ_{xy} to estimate γ . Correspondingly, using χ_{xy}^{ZF} would have required us to fit more data points around $\beta/2$ to calculate γ . In general, we need to use at least two data points for the χ_{xx} fit, and at least one data point for the χ_{xy}^{ZF} fit. When numerical errors are large, we choose to include more data points in order to obtain an accurate fit. The downside of including points further away from $\tau = \beta/2$ is that we must assume Drude-type behavior holds on a wider frequency range for σ_{xx} and σ_{xy} . Note that $\chi_{xx}(\tau)$ and $\chi_{xy}^{\text{ZF}}(\tau)$ are symmetric and antisymmetric about $\tau = \beta/2$, respectively, so we only use data points on one side of $\tau = \beta/2$.

Regarding the proxy D $_{\gamma}$, for $U/t \leq 8$, only the points at $\tau = \beta/2$ and $\tau = \beta/2 - \beta/L$ are used in the fitting procedure, while For $U/t \geq 12$, points at $\tau = \beta/2, \tau = \beta/2 - \beta/L$ and $\tau = \beta/2 - 2 \times \beta/L$ are used. The error in γ and Ω_{xx} obtained from fitting χ_{xx} is neglected, because χ_{xx} has much smaller relative error than χ_{xy}^{ZF} . The error in Ω_{xy}/B obtained from fitting χ_{xy}^{ZF} is ± 1 standard error determined by jackknife resampling.

For the M-type proxy, when we calculate $\chi_{\alpha\beta}(i\omega_n)$, we use a cubic spline to fit $\chi_{\alpha\beta}(\tau)$ and insert 10000 sampling points on the imaginary time axis, and integrate the oscillatory function as a function of τ using the composite trapezoidal rule.

For proxy M1, the errors from $\chi_{xx}(i\omega_n)$ are neglected and the error bar is ± 1 standard error determined by

jackknife resampling of $\chi_{xy}^{\text{ZF}}(i\omega_n)$. The cubic spline extrapolation to $\omega_n = 0$ utilizes data on the first three non-zero ω_n . The error bars for proxy M2 are constructed by error propagation of the standard errors in $\chi_{xy}^{\text{ZF}}(i\omega_1)$ and $[\chi_{xx}(\tau = \beta/2)]^2$, which are themselves determined by jackknife resampling.

-
- [1] M. Gurvitch and A. T. Fiory, Resistivity of $\text{La}_{1.825}\text{Sr}_{0.175}\text{CuO}_4$ and $\text{YBa}_2\text{Cu}_3\text{O}_7$ to 1100K: Absence of saturation and its implications, *Phys. Rev. Lett.* **59**, 1337 (1987).
- [2] K. Takenaka, R. Shiozaki, S. Okuyama, J. Nohara, A. Osuka, Y. Takayanagi, and S. Sugai, Coherent-to-incoherent crossover in the optical conductivity of $\text{La}_{2-x}\text{Sr}_x\text{CuO}_4$: charge dynamics of a bad metal, *Phys. Rev. B* **65**, 092405 (2002).
- [3] Y. Ando, S. Komiya, K. Segawa, S. Ono, and Y. Kurita, Electronic phase diagram of high- T_c cuprate superconductors from a mapping of the in-plane resistivity curvature, *Phys. Rev. Lett.* **93**, 267001 (2004).
- [4] O. Gunnarsson, M. Calandra, and J. E. Han, Colloquium: Saturation of electrical resistivity, *Rev. Mod. Phys.* **75**, 1085 (2003).
- [5] N. Hussey, K. Takenaka, and H. Takagi, Universality of the Mott–Ioffe–Regel limit in metals, *Philosophical Magazine* **84**, 2847 (2004).
- [6] M. Calandra and O. Gunnarsson, Violation of Ioffe-Regel condition but saturation of resistivity of the high- T_c cuprates, *Europhys. Lett.* **61**, 88 (2003).
- [7] V. J. Emery and S. A. Kivelson, Superconductivity in bad metals, *Phys. Rev. Lett.* **74**, 3253 (1995).
- [8] J. Černe, M. Grayson, D. C. Schmadel, G. S. Jenkins, H. D. Drew, R. Hughes, A. Dabkowski, J. S. Preston, and P.-J. Kung, Infrared Hall effect in high- T_c superconductors: Evidence for non-Fermi-liquid Hall scattering, *Phys. Rev. Lett.* **84**, 3418 (2000).
- [9] S. Ono, S. Komiya, and Y. Ando, Strong charge fluctuations manifested in the high-temperature Hall coefficient of high- T_c cuprates, *Phys. Rev. B* **75**, 024515 (2007).
- [10] E. W. Huang, R. Sheppard, B. Moritz, and T. P. Devereaux, Strange metallicity in the doped Hubbard model, *Science* **366**, 987 (2019).
- [11] R. Blankenbecler, D. J. Scalapino, and R. L. Sugar, Monte Carlo calculations of coupled boson-fermion systems. i, *Phys. Rev. D* **24**, 2278 (1981).
- [12] S. R. White, D. J. Scalapino, R. L. Sugar, E. Y. Loh, J. E. Gubernatis, and R. T. Scalettar, Numerical study of the two-dimensional Hubbard model, *Phys. Rev. B* **40**, 506 (1989).
- [13] W. Xu, W. McGehee, W. Morong, and B. DeMarco, Bad-metal relaxation dynamics in a Fermi lattice gas, *Nat. Commun.* **10**, 1588 (2019).
- [14] P. T. Brown, D. Mitra, E. Guardado-Sanchez, R. Nourafkan, A. Reymbaut, C.-D. Hébert, S. Bergeron, A.-M. S. Tremblay, J. Kokalj, D. A. Huse, P. Schauß, and W. S. Bakr, Bad metallic transport in a cold atom Fermi-Hubbard system, *Science* **363**, 379 (2019).
- [15] W. O. Wang, J. K. Ding, B. Moritz, E. W. Huang, and T. P. Devereaux, DC Hall coefficient of the strongly correlated Hubbard model, *npj Quantum Materials* **5**, 51 (2020).
- [16] H. Y. Hwang, B. Batlogg, H. Takagi, H. L. Kao, J. Kwo, R. J. Cava, J. J. Krajewski, and W. F. Peck, Scaling of the temperature dependent Hall effect in $\text{La}_{2-x}\text{Sr}_x\text{CuO}_4$, *Phys. Rev. Lett.* **72**, 2636 (1994).
- [17] B. Keimer, S. A. Kivelson, M. R. Norman, S. Uchida, and J. Zaanen, From quantum matter to high-temperature superconductivity in copper oxides, *Nature* **518**, 179 (2015).
- [18] D. Veberič and P. Prelovšek, Temperature dependence of the Hall response in doped antiferromagnets, *Phys. Rev. B* **66**, 020408 (2002).
- [19] B. S. Shastry, B. I. Shraiman, and R. R. P. Singh, Faraday rotation and the Hall constant in strongly correlated Fermi systems, *Phys. Rev. Lett.* **70**, 2004 (1993).
- [20] T. D. Stanescu and P. Phillips, Nonperturbative approach to full mott behavior, *Phys. Rev. B* **69**, 245104 (2004).
- [21] F. F. Assaad and M. Imada, Hall coefficient for the two-dimensional Hubbard model, *Phys. Rev. Lett.* **74**, 3868 (1995).
- [22] P. Prelovšek and X. Zotos, Reactive Hall constant of strongly correlated electrons, *Phys. Rev. B* **64**, 235114 (2001).
- [23] E. Lange and G. Kotliar, Magnetotransport in the doped Mott insulator, *Phys. Rev. B* **59**, 1800 (1999).
- [24] W. F. Brinkman and T. M. Rice, Hall effect in the presence of strong spin-disorder scattering, *Phys. Rev. B* **4**, 1566 (1971).
- [25] A. Auerbach, Hall number of strongly correlated metals, *Phys. Rev. Lett.* **121**, 066601 (2018).
- [26] J. Jaklič and P. Prelovšek, Lanczos method for the calculation of finite-temperature quantities in correlated systems, *Phys. Rev. B* **49**, 5065 (1994).
- [27] E. Jeckelmann and H. Benthien, Dynamical density-matrix renormalization group, in *Computational Many-Particle Physics* (Springer-Verlag, Berlin Heidelberg, 2008) pp. 621–635.
- [28] E. Y. Loh, J. E. Gubernatis, R. T. Scalettar, S. R. White, D. J. Scalapino, and R. L. Sugar, Sign problem in the numerical simulation of many-electron systems, *Phys. Rev. B* **41**, 9301 (1990).
- [29] M. Jarrell and J. E. Gubernatis, Bayesian inference and the analytic continuation of imaginary-time quantum Monte Carlo data, *Physics Reports* **269**, 133 (1996).
- [30] O. Gunnarsson, M. W. Haverkort, and G. Sangiovanni, Analytical continuation of imaginary axis data for optical conductivity, *Phys. Rev. B* **82**, 165125 (2010).
- [31] V. Viswanath and G. Müller, *The Recursion Method: Application to Many-Body Dynamics*, Vol. 23 (Springer-Verlag, Berlin Heidelberg, 1994).

- [32] D. E. Parker, X. Cao, A. Avdoshkin, T. Scaffidi, and E. Altman, A universal operator growth hypothesis, *Phys. Rev. X* **9**, 041017 (2019).
- [33] N. H. Lindner and A. Auerbach, Conductivity of hard core bosons: A paradigm of a bad metal, *Phys. Rev. B* **81**, 054512 (2010).
- [34] A. Auerbach, Equilibrium formulae for transverse magnetotransport of strongly correlated metals, *Phys. Rev. B* **99**, 115115 (2019).
- [35] J. K. Ding, W. O. Wang, Y. Schattner, B. Moritz, E. W. Huang, and T. P. Devereaux, (unpublished).
- [36] G. D. Mahan, *Many-particle physics* (Springer, Boston, MA, 2000).
- [37] Note that the translational and reflection symmetries of the unperturbed Hamiltonian imply that the modification of the current operator by the magnetic field does not contribute to $\chi_{xy}(\mathbf{r}, \tau)$ to first order in B .
- [38] M. Itoh, An exact expression for the Hall conductivity in gauge-invariant form, *J. Phys. F: Met. Phys.* **14**, L89 (1984).
- [39] M. Itoh, Gauge-invariant theory of the Hall effect in a weak magnetic field, *J. Phys. F: Met. Phys.* **15**, 1715 (1985).
- [40] H. Fukuyama, H. Ebisawa, and Y. Wada, Theory of Hall Effect. I: Nearly Free Electron, *Progress of Theoretical Physics* **42**, 494 (1969).
- [41] F. F. Assaad, Depleted kondo lattices: Quantum Monte Carlo and mean-field calculations, *Phys. Rev. B* **65**, 115104 (2002).
- [42] J. Tukey, Bias and confidence in not quite large samples, *Ann. Math. Statist.* **29**, 614 (1958).
- [43] H. Kontani, Theory of infrared hall conductivity based on the fermi liquid theory: Analysis of high- T_c superconductors, *Journal of the Physical Society of Japan* **76**, 074707 (2007).
- [44] L. B. Rigal, D. C. Schmadel, H. D. Drew, B. Maiorov, E. Osquiguil, J. S. Preston, R. Hughes, and G. D. Gu, Magneto-optical evidence for a gapped Fermi surface in underdoped $\text{YBa}_2\text{Cu}_3\text{O}_{6+x}$, *Phys. Rev. Lett.* **93**, 137002 (2004).
- [45] J. Černe, D. Schmadel, L. Rigal, and H. Drew, Measurement of the infrared magneto-optic properties of thin-film metals and high temperature superconductors, *Review of Scientific Instruments* **74**, 4755 (2003).
- [46] J. Černe, D. C. Schmadel, M. Grayson, G. S. Jenkins, J. R. Simpson, and H. D. Drew, Midinfrared Hall effect in thin-film metals: Probing the Fermi surface anisotropy in Au and Cu, *Phys. Rev. B* **61**, 8133 (2000).
- [47] S. Badoux, W. Tabis, F. Laliberté, G. Grissonnanche, B. Vignolle, D. Vignolles, J. Béard, D. Bonn, W. Hardy, R. Liang, *et al.*, Change of carrier density at the pseudogap critical point of a cuprate superconductor, *Nature* **531**, 210 (2016).
- [48] C. Collignon, S. Badoux, S. A. A. Afshar, B. Michon, F. Laliberté, O. Cyr-Choinière, J.-S. Zhou, S. Licciardello, S. Wiedmann, N. Doiron-Leyraud, and L. Taillefer, Fermi-surface transformation across the pseudogap critical point of the cuprate superconductor $\text{La}_{1.6-x}\text{Nd}_{0.4}\text{Sr}_x\text{CuO}_4$, *Phys. Rev. B* **95**, 224517 (2017).
- [49] N. Doiron-Leyraud, O. Cyr-Choinière, S. Badoux, A. Ataei, C. Collignon, A. Gourgout, S. Dufour-Beauséjour, F. Tafti, F. Laliberté, M.-E. Boulanger, *et al.*, Pseudogap phase of cuprate superconductors confined by Fermi surface topology, *Nat. Commun.* **8**, 2044 (2017).
- [50] A. Reymbaut, D. Bergeron, and A.-M. S. Tremblay, Maximum entropy analytic continuation for spectral functions with nonpositive spectral weight, *Phys. Rev. B* **92**, 060509 (2015).
- [51] A. Reymbaut, A.-M. Gagnon, D. Bergeron, and A.-M. S. Tremblay, Maximum entropy analytic continuation for frequency-dependent transport coefficients with nonpositive spectral weight, *Phys. Rev. B* **95**, 121104 (2017).
- [52] J. Fei, C.-N. Yeh, and E. Gull, Nevanlinna analytical continuation, *Phys. Rev. Lett.* **126**, 056402 (2021).
- [53] J.-H. Sim and M. J. Han, Maximum quantum entropy method, *Phys. Rev. B* **98**, 205102 (2018).
- [54] Y. Burnier and A. Rothkopf, Bayesian approach to spectral function reconstruction for euclidean quantum field theories, *Phys. Rev. Lett.* **111**, 182003 (2013).
- [55] A. Rothkopf, Bayesian inference of nonpositive spectral functions in quantum field theory, *Phys. Rev. D* **95**, 056016 (2017).